

Probing evaporation induced assembly across a drying colloidal droplet using *in situ* small-angle X-ray scattering at the synchrotron source†

Cite this: *Soft Matter*, 2014, 10, 1621D. Sen,^{*a} J. Bahadur,^a S. Mazumder,^a G. Santoro,^b S. Yu^b and S. V. Roth^b

Colloidal particles in a tiny drying droplet are forced to assemble due to attractive capillary forces. Jamming of the particles throughout the droplet remains either isotropic or anisotropic depending upon the drying kinetics and the physicochemical environment. In this work, we explore the dynamical evolution of such an assembly process across a single evaporative droplet by *in situ* scanning small-angle scattering using a micro-focused X-ray beam at the synchrotron source. A methodology has been elucidated to differentiate quantitatively between the isotropic and the anisotropic jamming process. Switching of jamming behaviour depending on the initial particle volume fraction in the droplet has been demonstrated. Three distinct stages of assembly, associated with droplet shrinkage, have been revealed even during isotropic jamming. This is in contrast to the drying of a pure liquid droplet under diffusion limited evaporation. It has been established that such *in situ* scattering measurements can also be used to estimate the temporal evolutions of the viscosity of a drying suspension as well as the diffusivity of nanoparticles in a droplet.

Received 29th July 2013

Accepted 9th December 2013

DOI: 10.1039/c3sm52039k

www.rsc.org/softmatter

Introduction

Evaporation of fluids from a drying suspension droplet forces tiny particles to organize through attractive capillary forces.^{1–3} Such evaporative drying eventually leads to the formation^{4–10} of correlated nano-structured^{11,12} hierarchical grains. It is worth mentioning that droplet drying^{13,14} is ubiquitous and of practical interest too in various industrial processes such as spray drying with application in food processing, pharmaceuticals, ceramics, detergents, *etc.* In recent past, evaporation induced assembly of nanostructures through droplet drying has been realized^{4–6,15,16} to synthesize nanocomposite grains with controlled morphologies and also devices for optical photovoltaic cells.¹⁷ Very recently, the potential use of such assembled *E. coli* template hollow porous grains in filtration applications has been demonstrated¹⁸ by our group.

Drying drives the initial suspension far from equilibrium and such a process of dynamical organization poses a number of intriguing fundamental issues related to the nature of jamming of the nanoparticles. One of the interesting aspects in this regard is to ascertain whether the jamming of particles is isotropic or anisotropic throughout the droplet. This is important in order to differentiate the mechanisms of formation of

uniformly jammed grains, hollow grains having jammed shells and the grains with a gradient in particle jamming. To date, a few attempts have been made to comprehend such organization of tiny particles in droplets, either in sessile^{7,13,14,19–26} or in spray form,²⁷ once the pioneering coffee ring effect^{1,2} was discovered. Buckling^{7,28} of thin elastic shells formed by interlocking of the organized particles was elucidated and explained in terms of viscoelastic transition of the droplet shell at faster drying rate. On the other hand, scattering experiments²⁷ on spray droplets under a slower drying regime shed light on isotropic shrinkage of spray droplets. However, the temporal evolution of the organization process *vis-à-vis* the measurement of the concentration field across a drying droplet still remains unanswered. For an ideal liquid droplet, without any suspended particles, shrinkage due to diffusion limited evaporation is given by²⁹ square law type temporal variation, *i.e.*, $[R_0^2 - R^2(t)] \propto t$, where R_0 and $R(t)$ are the radius of an initial droplet and that at time t , respectively. This implies a constant shrinkage rate throughout the entire shrinking process. However, experimental evidence about the validity of the above law in a drying suspension droplet is of great interest. Efforts were made to investigate the effects^{30,31} during solvent evaporation in thin films where variation in volume fraction was measured indirectly from the weight change of a drying film. Transmitted light attenuation measurements were performed³² on sessile droplets in order to identify self-pinning and variation in particle concentration where contact line pinning and particle substrate adhesion is significant enough in deciding the particle assembly unlike that of a spherical spray droplet.

^aSolid State Physics Division, Bhabha Atomic Research Centre, Mumbai-400085, India.
E-mail: debasis@barc.gov.in

^bDeutsches Elektronen-Synchrotron (DESY), Notkestr. 85 D-22607, Hamburg, Germany

† Electronic supplementary information (ESI) available. See DOI: 10.1039/c3sm52039k

Small-angle scattering is an important and well established nondestructive technique for investigating mesoscopic structure assembly³³ in condensed matter. In this work, we report the investigations on *in situ* evolution of nanoparticle organization in single evaporative droplets using scanning small-angle X-ray scattering (SAXS) at the synchrotron source. We demonstrate that such an experiment can be used to differentiate quantitatively between the isotropic and anisotropic jamming. We were able to map the radial concentration gradient across a droplet and corroborate the results by model calculations. The presence of three distinct stages during droplet shrinkage unlike the constant rate for a pure liquid droplet is revealed. As the experiment is conducted on a single droplet, the smearing of scattering information by droplet polydispersity²⁷ does not arise at all. *In situ* scattering experiment³⁴ on an evaporative droplet, using a micro-focused synchrotron beam in scanning mode, is best suited to address the above issues as it can probe simultaneously the evolution of droplet shrinkage and nanoparticle concentration.³⁵

Experimental

Nearly a 1 μL colloidal droplet, hanging from a narrow tip, was generated using silica colloidal dispersion (SM 30, LUDOX®, average particle radius of ~ 5 nm). The weight percent of the silica in the as-received aqueous dispersion was 30%. The tip was attached to an XYZ translational stage, controlled remotely. The initial volume fraction (ϕ_0) of nanoparticles in the droplet was kept either at 0.015 or at 0.15. The required amount of dispersion was taken into the tip using a micropipette and a droplet was formed using the whole amount of dispersion in order to rule out the possibility of further dispersion drawn down into the droplet. *In situ* SAXS experiments on such evaporative droplets were performed at the Micro and Nano focus X-ray Scattering beamline P03 (MiNAXS) at the synchrotron source PETRA-III, DESY, Hamburg, Germany.^{13,36} The beam size for SAXS measurements was $32\text{ }\mu\text{m}$ (H) \times $23\text{ }\mu\text{m}$ (V) with a wavelength of 0.0957 nm . All experiments were performed under ambient conditions ($T = 25\text{ }^\circ\text{C}$ and relative humidity 40%). Scattering images were recorded using a 2D-pixel detector (Pilatus 300k, DECTRIS, Switzerland) and the radial averaged intensity $I(q)$ was calculated for different wave vector transfers (q). Beamline hutch searching and finding droplet centre by X-ray transmission took typical five minutes in each case. Thus, the starting time of each experiment ($t = 0$) is effectively five minutes later as far as the formation of droplets was concerned. Further, standard time independent SAXS experiments on colloidal dispersions, filled in a 1 mm quartz capillary tube, were also carried out, using a laboratory based SAXS instrument.

Results and discussion

In situ experiments (Fig. 1a) were performed in two different modes: (i) either by scanning across the droplet during the drying process or (ii) by monitoring of the evolution of the scattering profile at a fixed position. The choice of the present colloidal suspension is motivated by its good stability and relatively low

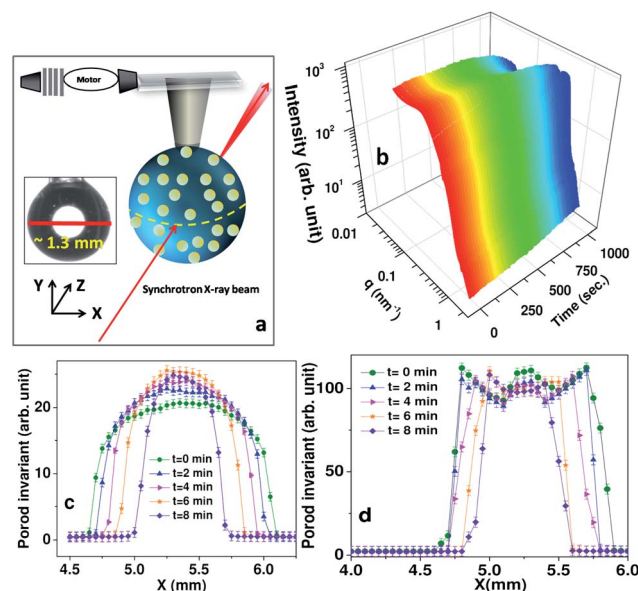


Fig. 1 (a) Schematic diagram of experimental configuration. The inset shows an optical image of a hanging droplet. (b) Evolution of the SAXS profile during isotropic jamming. Spatial variation of Porod invariant across the droplet for: (c) isotropic and (d) anisotropic jamming.

size polydispersity ($\sim 10\%$). Further, for *in situ* experiments, a good scattering contrast is an important factor as far as the intensity of the scattering is concerned. Silica has a reasonably good X-ray scattering contrast. We used the same nanoparticle for two different initial concentrations in order to make the comparison more realistic by keeping the particle size constant.

To map the concentration field inside the droplet, Porod invariant $Q = \int_0^\infty I(q)q^2 dq$ from each scattering profile was estimated. It is worth mentioning that Porod invariant is an important quantity that can be obtained from SAXS data and characterizes the total scattering power of the density fluctuations present in the sample. It is observed from Fig. 1c that for an initial ϕ of 0.015, Q along a chord falls off symmetrically about the vertical symmetry axis. The variation of Q across the droplet is bell shaped and is convex upward. As time passes, the width of the curve decreases because of droplet shrinkage. Interestingly, the spatial variation of Q across the droplet changes dramatically for higher value of initial ϕ (Fig. 1d). It is evident that unlike the previous case, Q shows a strikingly different trend in the intermediate range.

In order to understand the difference in shape of the spatial Q variation in both cases, an analytical approach has been adopted. Q corresponding to any point of incidence across a fixed chord must be proportional to the total volume of effective X-ray beam path through the colloidal droplet. It is to be noted that in the present case, the scanning rate is higher than the drying rate of the droplet. If the jamming is isotropic and the nanoparticles are distributed homogeneously (with volume fraction ϕ) throughout the droplet, the effective Q is proportional to $\phi(1 - \phi)(R^2 - x^2)^{0.5}$ (see ESI†), where R is the instantaneous radius of the droplet and x is the perpendicular distance from the droplet centre to the X-ray beam through the droplet.

Thus, in such a situation, the spatial variation of Q represents a bell shaped curve (Fig. 2a) which is convex upward as is experimentally observed (Fig. 1c).

Using a simplistic model, preferred isotropic jamming may occur when the mixing time of the colloidal particles τ_{mix} is smaller than the drying time τ_d *i.e.* when the ratio of $\tau_{\text{mix}}/\tau_d \leq 1$. On the other hand if $\tau_{\text{mix}}/\tau_d \gg 1$, it is expected that the particles get hardly any time to mix and in this case the assembly will not be isotropic and may lead to the following scenario: nanoparticles form a jammed shell at the air–water interface and the core remains at lower ϕ . In this case, Q can be expressed as (see ESI†).

$$Q \propto \begin{cases} 2\phi_1(1-\phi_1)(R_i^2 - x^2)^{0.5} + 2\phi_2(1-\phi_2) \frac{(R_o^2 - R_i^2)}{[(R_o^2 - x^2)^{0.5} + (R_i^2 - x^2)^{0.5}]} & \text{for } x < R_i \\ 2\phi_2(1-\phi_2)(R_o^2 - x^2)^{0.5} & \text{for } R_i < x < R_o \end{cases}$$

where R_i and R_o are inner and outer radii of the drying droplet and ϕ_1 and ϕ_2 are volume fractions of the nanoparticles in core and shell, respectively. It is worth mentioning that in reality, in an intermediate situation, a radial gradient field of jamming concentration may arise. For grains with jammed shell and hollow core, the Q variation shows a clear dip in-between unlike that for the isotropic case. For a jammed shell with core at relatively low ϕ , the situation lies in-between the above mentioned two extreme cases: a uniform volume fraction inside the droplet and a droplet comprised of a colloidal shell and a hollow core. As the number of total colloids (N_0) in a droplet remains constant during drying, $N_{\text{shell}}(t) + N_{\text{core}}(t) = N_0$ implying that the volume fractions of the core and shell are related to each other according to the following expression.

$$\phi_{\text{shell}} \frac{4}{3} \pi (R_{\text{out}}^3 - R_{\text{in}}^3) + \phi_{\text{core}} \frac{4}{3} \pi (R_{\text{in}}^3) = \phi_0 \frac{4}{3} \pi R_0^3$$

and thus $\phi_{\text{shell}}(t) = \frac{\phi_0 R_0^3 - \phi_{\text{core}}(t) R_{\text{in}}^3(t)}{[R_{\text{out}}^3(t) - R_{\text{in}}^3(t)]}$. Experimental variations of Porod invariant are compared to the above model (Fig. 3).

For a droplet of radius R , τ_{mix} is equal to R^2/D ,⁷ where D is the diffusion co-efficient of the nanoparticles in a droplet. Using the Stokes–Einstein equation, D at temperature T can be expressed by $D = kT/(6\pi\eta r_p)$ with η being the fluid viscosity and r_p the radius of

the nanoparticles. In fact, the viscosity of the colloidal suspension is a function of colloidal volume fraction (ϕ) and can be expressed as $\eta(\phi) \propto \left(1 - \frac{\phi}{2}\right)(1 - \phi)^{-3}$ (ref. 37). Using the above equations and with $r_p = 5$ nm, $\eta = 9.2 \times 10^{-4}$ Pa s (for the initial dilute aqueous suspension with ϕ equal to 0.015, as estimated using the above equation and taking the viscosity of pure water at 25 °C as 8.9×10^{-4} Pa s (ref. 38)), D becomes 4.7×10^{-11} m² s⁻¹. For $\tau_d = 12$ min and initial droplet radius 0.65 mm, the ratio τ_{mix}/τ_d becomes 12. Although the ratio of the mixing time to the drying time is significantly higher than 1, isotropic jamming

occurred during evaporation. However, for a droplet with the same volume but with initial ϕ of 0.15, where the estimated initial diffusion coefficient is 3.3×10^{-11} m² s⁻¹ and $\tau_{\text{mix}}/\tau_d \approx 25$, anisotropic jamming arose. This implies that a simple model, based on the mere ratio of τ_{mix}/τ_d , is not enough to describe the drying process completely, implying consideration of drying temperature dependent hydrodynamics and non-equilibrium modeling for estimation of the effective mixing time.

The present results indicate that even if the Peclet number is significantly higher than unity, still a uniform assembly is possible at low initial particle concentration and with low drying temperature unlike the former observation³⁰ on drying of thin films where consideration of the contact line pinning and particle substrate adhesion is significant enough in deciding the particle assembly unlike that of a spherical droplet.

As the real space and the reciprocal space are connected by Fourier transform, the regime at relatively higher q primarily bears the information about smaller density fluctuations (*i.e.*, the morphology and the correlation of the silica particles in the droplet). The low q regime mainly contains the information about the larger length scale *i.e.*, scattering from relevant zones from overall droplets.

$$\text{So, } I(q) = I_{\text{silica}}(a) + I_{\text{droplet}}(q).$$

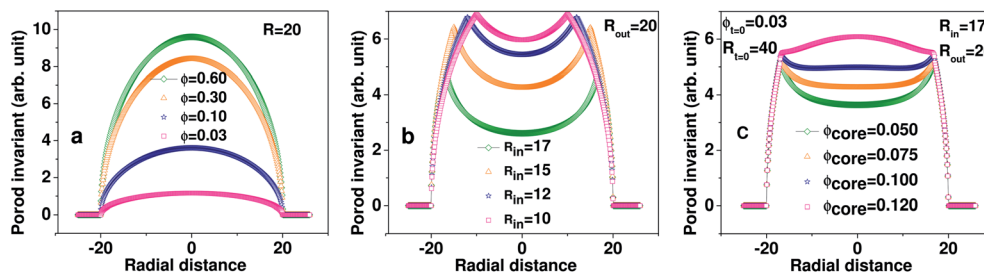


Fig. 2 Simulated variation of Q for (a) droplet with uniform ϕ , (b) assembled grain with a colloidal shell and hollow core, and (c) droplet with different ϕ at its shell (0.55, 0.50, 0.46, and 0.43 respectively) and its core.

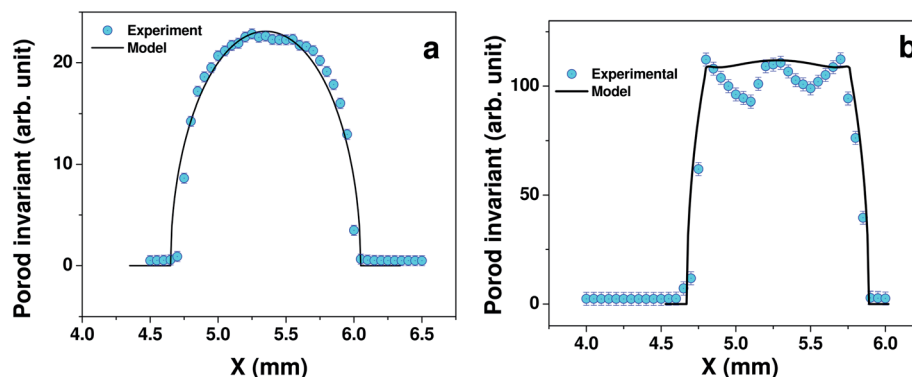


Fig. 3 (a) Comparison of model and experimental data for the isotropic case and (b) comparison of model and experimental data for the anisotropic case. We could reproduce the tendency of spatial behaviour. Slight mismatch between the model and the experiment is attributed to the local gradient and fluctuation of the volume fraction.

For uniform correlation throughout the droplet under local monodisperse approximation³⁹

$$I_{\text{silica}}^{\text{uniform}}(q) = C \int_0^\infty P_{\text{silica}}(q, r) v_{\text{silica}}^2(r) D_{\text{silica}}(r) S_{\text{uniform}}(q) dr.$$

$P(q, r)$ represents the form factor for silica particles with radius r (and volume $v(r)$). $D_{\text{silica}}(r)$ represents the size distribution of the silica particles. $S(q)$ represents the inter-particle structure factor. C is a q independent scale factor that is related to scattering contrast.

However, for the anisotropic jamming case, consideration of two types of silica correlations in the droplet were necessary for explaining the SAXS data.

$$I_{\text{silica}}^{\text{anisotropic}}(q) = C_1 \left(\int_0^\infty P_{\text{silica}}(q, r) v_{\text{silica}}^2(r) D_{\text{silica}}(r) S_{\text{core}}(q) dr \right) + C_2 \left(\int_0^\infty P_{\text{silica}}(q, r) v_{\text{silica}}^2(r) D_{\text{silica}}(r) S_{\text{shell}}(q) dr \right)$$

The contribution for $I_{\text{droplet}}(q)$ was approximated to $I_{\text{droplet}}(q) \approx Kq^{-n}$ and significant only in a very low q regime. During fitting the experimental data, it was found that a hard sphere/sticky hard sphere type structure factor^{40–42} with local monodisperse approximation³⁹ fits reasonably well. For higher volume fraction a sticky hard sphere type structure factor represents better fit.

For the isotropic case, as the ϕ of the nanoparticles in the droplet is uniform throughout, SAXS profiles (Fig. 4a) resemble the scattering from ensembles of nanoparticles at uniform volume fraction. However, for the anisotropic case, with initial $\phi = 0.15$, profiles (Fig. 4a) could not be explained for the uniform volume fraction but contributions from ensembles of particles having two different ϕ values (0.16 and 0.66) inside the drying droplet represent the data fairly well. This observation further affirms the difference in the spatial variation of Q in the two cases mentioned above.

To differentiate the effects of drying on the scattering profiles of the colloids in droplets, we also performed the

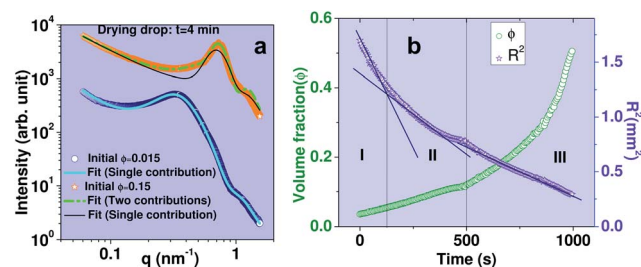


Fig. 4 (a) SAXS analysis shows that for low initial concentration, nanoparticles assemble uniformly throughout the droplet during drying (e.g. $\phi = 0.04$ at $t = 4$ min). For higher initial concentration, assembly is not uniform but two different values of ϕ i.e., at core and shell ($\phi = 0.16$ at core and $\phi = 0.66$ at shell at $t = 4$ min) of drying droplets are indicated. (b) Evolution of volume fraction (ϕ) and square of droplet size (R) in the case of isotropic jamming. Three stages of droplet shrinkage are evident unlike the single stage diffusion-limited shrinkage of pure liquid droplets.

experiments on standard capillary cells for dilute as well as concentrated dispersions. It is to be noted that the drying effect is negligible in this case. Interestingly, it is observed that even for the concentrated dispersion, the scattering profiles corroborate quite well (Fig. 5) with the model of uniform colloidal volume fractions. This is in contrast to the situation for the concentrated droplet where the drying effect is prominent. The estimated form factor and structure factors are shown in the ESI (Fig. S4†).

Now, we would like to discuss the evolution of nanoparticle volume fraction and evolution of droplet radius. Using *in situ* monitoring of the scattering profile at a fixed position of droplets for the isotropic shrinkage case, the evolution of the droplet radius may be estimated from the mass balance equation $R_k^2 = R_0^2 \left(\frac{\phi_i}{\phi_k} \right)^{2/3}$ where R and ϕ represent the radius of the droplet and the corresponding volume fraction of the particles with i and k representing the initial and any intermediate stage, respectively. The value of ϕ , at different times, was estimated from fitting of the model to the scattering data. Temporal evolution of ϕ_k and R_k is depicted in Fig. 4b. It is interesting to

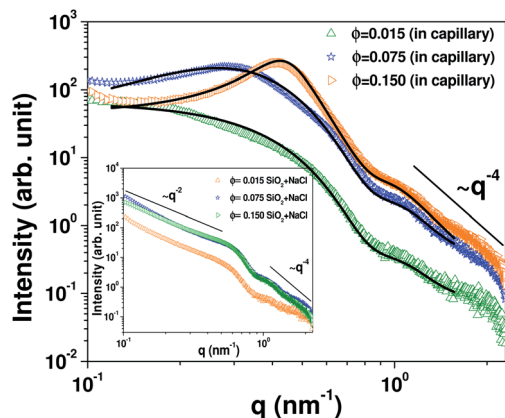


Fig. 5 SAXS profiles from bulk colloidal dispersion for $\phi = 0.015$, 0.075 and 0.150. The experimental data corroborate quite well with the model (solid line) of uniform colloidal volume fraction. The inset shows the SAXS curves of the bulk colloids after destabilization by sodium chloride.

observe that unlike the drying of a pure liquid droplet, where only a single linear zone appears²⁹ for droplet shrinkage with $[R_0^2 - R^2(t)] = Ct$, the evolution of R^2 in the present case is not linear with time and encompasses three distinct temporal zones. Furthermore, it is observed that the droplet shrinkage rate chronologically decreases from stage-I to stage-III. The evaporation rate in stage I ($C_1 = 4.0 \times 10^{-3} \text{ mm}^2 \text{ s}^{-1}$) is significantly higher than that in stage II ($C_2 = 1.0 \times 10^{-3} \text{ mm}^2 \text{ s}^{-1}$) and stage III ($C_3 = 9.1 \times 10^{-4} \text{ mm}^2 \text{ s}^{-1}$). This can be understood as follows. After the initial stage, water can evaporate only through the channels formed by the interstices of the nanoparticles, leading to lower evaporation rate. At the last stage, when the jamming of the nano-particles dominates, the remaining trapped water in the nano-channels evaporates at further slow rate.

Variations of relative viscosity as well as diffusion coefficient, estimated from the variation of ϕ , are plotted in Fig. 6.

The relative diffusion coefficient also shows three distinct temporal stages of evolution. It is evident that diffusion of the nanoparticles reduces as a natural consequence with time. However, the rate of decrease of the same increases with time as

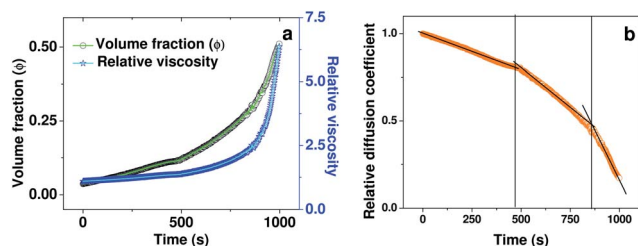


Fig. 6 (a) Temporal variation of relative viscosity during drying is compared to the functional variation of volume fraction. (b) Temporal variation of the relative diffusion coefficient normalized to $t = 0 \text{ s}$ as estimated from the evolution of viscosity. Three stages of variation are also evident for the diffusion coefficient.

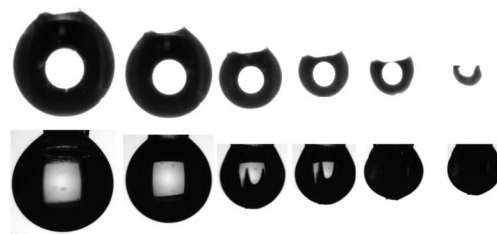


Fig. 7 (a) Optical images showing the evolution of drying droplets. The top row represents the images of the droplets with initial $\phi = 0.015$ and the bottom row represents the images of the droplets with initial $\phi = 0.15$. The appearance of the non-reflective surface for the bottom row images at later times is evident.

the interparticle distance starts decreasing with passage of time.

Here we would like to present the optical images (Fig. 7) of drying droplets for two different initial concentrations of the colloids. The trapping of the particles due to the formation of a shell at higher initial concentration is evident from the non-reflective droplet surface at later times.

We would like to mention at this juncture that the present study demonstrates that such *in situ* SAXS measurements, on a drying colloidal droplet, may be performed to monitor the evolution of the suspension viscosity and diffusivity of the nanoparticles within the drying droplet. Such measurements with a faster scanning rate and with a further focused synchrotron beam may be useful in order to address the issue of buckling^{7,15,43} of a jammed colloidal shell during rapid spray drying that involves viscoelastic transition during drying.

Conclusions

In summary, we have demonstrated that isotropic and anisotropic evaporation induced assembly processes in a drying droplet can be differentiated directly from the measurement of the concentration field across the droplet through *in situ* scanning SAXS measurements using a narrow synchrotron beam. An analytical calculation has been accomplished to evaluate the nature of concentration gradient across the drying droplet from the SAXS data. The dependence of jamming behavior on the initial colloidal concentration and the existence of three distinct stages during isotropic jamming has been experimentally verified. Such three-stage evolution is in sharp contrast to the single stage diffusion-limited shrinkage of a pure liquid droplet. The present results show that even if the Peclet number remains significantly higher than unity, isotropic assembly is still possible at low enough initial concentration of the nanoparticles and at low drying temperature. This indicates the necessity of improvisation of an effective theoretical model to differentiate the isotropic and anisotropic evaporation induced assembly, which at present is based on the mere ratio of mixing to drying time. Our methodology illustrates the capability of revealing the structural gradient inside nanostructured micrometric spray-dried granules using scanning SAXS with focused X-ray beam. In addition, the present dynamical SAXS measurements propose a

methodology for estimating the evolution of the viscosity of a micrometric drying dispersion-droplet and diffusivity of nanoparticles in the droplet, which may find application in controlling the morphology of nanostructured micro-granules synthesized through spray drying, an indispensable technique in numerous industries.

Acknowledgements

DS and JB thankfully acknowledge the Department of Science and Technology (DST), India for providing financial support (1-20110533) for the experiment at PETRA-III, through Saha Institute of Nuclear Physics (SINP), Kolkata, India. SY acknowledges financial support from the Knut and Alice Wallenberg foundation (Sweden). This work was carried out at the P03 beamline of the light source PETRA III at DESY. DESY is a member of the Helmholtz Association (HGF). DS thanks Drs A. Thill and O. Spalla, for many useful discussions on spray drying during his visit to CEA, Saclay, France. DS thanks Dr A. Ghosh, DD, BARC for his help in obtaining some of the optical images.

References

- 1 R. D. Deegan, O. Bakajin, T. F. Dupont, G. Huber, S. R. Nagel and T. A. Witten, *Nature*, 1997, **389**, 827–829.
- 2 N. D. Denkov, O. D. Velev, P. A. Kralchevsky, I. B. Ivanov, H. Yoshimura and K. Nagayama, *Nature*, 1993, **361**, 26.
- 3 P. J. Yunker, T. Still, M. A. Lohr and A. G. Yodh, *Nature*, 2011, **476**, 308–311.
- 4 F. Iskandar, Mikrajuddin and K. Okuyama, *Nano Lett.*, 2001, **1**, 231–234.
- 5 D. Sen, J. Bahadur, S. Mazumder, G. Verma, P. A. Hassan, S. Bhattacharya, K. Vijai and P. Doshi, *Soft Matter*, 2012, **8**, 1955–1963.
- 6 D. Sen, J. S. Melo, J. Bahadur, S. Mazumder, S. Bhattacharya, S. F. D'Souza, H. Frielinghaus, G. Goerigk and R. Loidl, *Soft Matter*, 2011, **7**, 5423–5429.
- 7 N. Tsapis, E. R. Dufresne, S. S. Sinha, C. S. Riera, J. W. Hutchinson, L. Mahadevan and D. A. Weitz, *Phys. Rev. Lett.*, 2005, **94**, 0183021–0183024.
- 8 E. Tijerino, S. Basu and R. Kumar, *J. Appl. Phys.*, 2013, **113**, 034307.
- 9 S. Hu, J. Rieger, Y. Lai, S. V. Roth, R. Gehrke and Y. Men, *Macromolecules*, 2008, **41**, 5073–5076.
- 10 V. Körstgens, J. Wiedersich, R. Meier, J. Perlich, S. V. Roth, R. Gehrke and P. Müller-Buschbaum, *Anal. Bioanal. Chem.*, 2010, **396**, 139–149.
- 11 K. Rykaczewski, J. Chinn, M. L. Walker, J. H. J. Scott, A. Chinn and W. Jones, *ACS Nano*, 2011, **5**, 9746–9754.
- 12 H. Wang, X. Zhu, L. Tsarkova, A. Pich and M. Möller, *ACS Nano*, 2011, **5**, 3937–3942.
- 13 S. V. Roth, G. Herzog, V. Körstgens, A. Buffet, M. Schwartzkopf, J. Perlich, M. M. A. Kashem, R. Döhrmann, R. Gehrke, A. Rothkirch, K. Stassig, W. Wurth, G. Benecke, C. Li, P. Fratzl, M. Rawolle and P. Müller-Buschbaum, *J. Phys: Cond. Matter*, 2011, **23**, 254208.
- 14 S. V. Roth, T. Autenrieth, G. Grübel, C. Riekel, M. Burghammer, R. Hengstler, L. Schulz and P. Müller-Buschbaum, *Appl. Phys. Lett.*, 2007, **91**, 091915.
- 15 J. Bahadur, D. Sen, S. Mazumder, S. Bhattacharya, H. Frielinghaus and G. Goerigk, *Langmuir*, 2011, **27**, 8404–8414.
- 16 M. Al-Hussein, M. Schindler, M. A. Ruderer, J. Perlich, M. Schwartzkopf, G. Herzog, B. Heidmann, A. Buffet, S. V. Roth and P. Müller-Buschbaum, *Langmuir*, 2013, **29**, 2490–2497.
- 17 R. A. Alaa, K. S. Viridi, R. Meier, M. Döblinger, P. Müller-Buschbaum, C. Scheu, P. Lugli and G. Scarpa, *Adv. Funct. Mat.*, 2012, **22**, 4078–4086.
- 18 J. S. Melo, D. Sen, S. Mazumder and S. F. D'Souza, *Soft Matter*, 2013, **9**, 805.
- 19 S. Narayanan, J. Wang and X.-M. Lin, *Phys. Rev. Lett.*, 2004, **93**, 135503.
- 20 J. Xu, J. Xia, S. W. Hong, Z. Lin, F. Qiu and Y. Yang, *Phys. Rev. Lett.*, 2006, **96**, 066104.
- 21 L. Xu, A. Bergès, P. J. Lu, A. R. Studart, A. B. Schofield, H. Oki, S. Davies and D. A. Weitz, *Phys. Rev. Lett.*, 2010, **104**, 128303.
- 22 L. Yang, Y. Zhang, J. Luo, Y. Luo, K. Gao, D. Li and Q. Meng, *Phys. Rev. E*, 2011, **84**, 031605.
- 23 J. Leng, *Phys. Rev. E*, 2010, **82**, 021405.
- 24 Á. G. Marín, H. Gelderblom, D. Lohse and J. H. Snoeijer, *Phys. Rev. Lett.*, 2011, **107**, 085502.
- 25 M. Kuhlmann, J. M. Feldkamp, J. Patommel, S. V. Roth, A. Timmann, R. Gehrke, P. Müller-Buschbaum and C. G. Schroer, *Langmuir*, 2009, **25**, 7241.
- 26 T. P. Bigoni, X.-m. Lin, T. Nguyen, E. I. Corwin, T. A. Witten and H. M. Jaeger, *Nat. Mater.*, 2006, **5**, 265–270.
- 27 D. Sen, O. Spalla, O. Taché, P. Haltebourg and A. Thill, *Langmuir*, 2007, **23**, 4296–4302.
- 28 L. Pauchard and Y. Couder, *Europhys. Lett.*, 2004, **66**, 667.
- 29 *Dynamics of droplets*, ed. A. Frohn and N. Roth, Springer-Verlag, Berlin, 2000.
- 30 T. Narita, P. Hebraud and F. Lequeux, *Eur. Phys. J. E Soft Matter*, 2005, **17**, 69–76.
- 31 A. F. Routh and W. B. Zimmerman, *Chem. Eng. Sci.*, 2004, **59**, 2961–2968.
- 32 D. M. Kuncicky and O. D. Velev, *Langmuir*, 2008, **24**, 1371–1380.
- 33 T. Paik, D.-K. Ko, T. R. Gordon, V. Doan-Nguyen and C. B. Murray, *ACS Nano*, 2011, **5**, 8322–8330.
- 34 A. Accardo, M. Burghammer, E. D. Cola, M. Reynolds, E. D. Fabrizio and A. C. Riekel, *Langmuir*, 2011, **27**, 8216–8222.
- 35 P. Wette, I. Klassen, D. Holland-Moritz, D. M. Herlach, H. J. Schöpe, N. Lorenz, H. Reiber, T. Palberg and S. V. Roth, *J. Chem. Phys.*, 2010, **132**, 131102.
- 36 A. Buffet, A. Rothkirch, R. Döhrmann, V. Körstgens, M. M. A. Kashem, J. Perlich, G. Herzog, M. Schwartzkopf, R. Gehrke, P. Müller-Buschbaum and S. V. Roth, *J. Synchr. Radiation*, 2012, **19**, 647.

- 37 R. Verberg, I. M. d. Schepper and E. G. D. Cohen, *Phys. Rev. E*, 1997, **55**, 3143–3158.
- 38 J. Kestin, M. Sokolov and W. A. Wakeham, *J. Phys. Chem. Ref. data*, 1978, **7**, 941–948.
- 39 J. S. Pedersen, *J. Appl. Cryst.*, 1994, **27**, 595–608.
- 40 N. W. Aschroft and J. Lekner, *Phys. Rev.*, 1966, **145**, 83–90.
- 41 R. J. Baxter, *J. Chem. Phys.*, 1968, **49**, 2770–2774.
- 42 S. V. G. Menon, C. Manohar and K. S. Rao, *J. Chem. Phys.*, 1991, **95**, 9186–9190.
- 43 D. Sen, J. S. Melo, J. Bahadur, S. Mazumder, S. Bhattacharya, G. Ghosh, D. Dutta and S. F. D'Souza, *Eur. Phys. J. E Soft Matter*, 2010, **31**, 393–402.